Journal of MATERIALS RESEARCH

Article
DOI: 10.1557/jmr.2019.352

General strategy for doping rare earth metals into Au–ZnO core–shell nanospheres

René Zeto[1], Daniel Cummins[2], Arynn Gallegos[3], Mike Shao[1], Andrea M. Armani[4,a)]

[1]Mork Family Department of Chemical Engineering and Materials Science, University of Southern California, Los Angeles, California 90089, USA
[2]Department of Biomedical Engineering, University of Southern California, Los Angeles, California 90089, USA
[3]Ming Hsieh Department of Electrical and Computer Engineering, University of Southern California, Los Angeles, California 90089, USA
[4]Mork Family Department of Chemical Engineering and Materials Science, University of Southern California, Los Angeles, California 90089, USA; Department of Biomedical Engineering, University of Southern California, Los Angeles, California 90089, USA; and Ming Hsieh Department of Electrical and Computer Engineering, University of Southern, Los Angeles, California 90089, USA
a)Address all correspondence to this author. e-mail: armani@usc.edu

Received: 14 August 2019; accepted: 30 October 2019

Multifunctional nanoparticles are an emerging area of research, impacting numerous fields ranging from biomedical applications to energy. While initial core–shell structures consisted of similar materials, such as Au–Ag or CdTe–CdSe nanoparticles, recent work has expanded this line of investigation to include particles of dissimilar materials. However, there are several challenges when synthesizing dissimilar material systems. In this work, a method for doping the shell of an Au–ZnO nanosphere is demonstrated. Several metal dopants are investigated, including Cu, Ce, Er, Nd, Tm, and Yb. The ZnO shell is nucleated on the gold nanosphere core via an ascorbic acid–assisted growth, and the dopant is intercalated uniformly into the shell during the self-assembly phase of the shell formation. The doping and polycrystalline shell are confirmed using a series of qualitative and quantitative methods. This multi-material nanoparticle synthesis strategy opens the door for future applications in sensing, photocatalysis, and bioimaging.

Introduction

The core–shell nanoparticle forms the foundation of many modern nanomaterial-based technologies. The initial motivation for creating a shell was to protect the functional core; the canonical example being the core–shell quantum dot [1, 2, 3]. More recently, researchers have begun expanding the role of the shell in this structure by developing particles with functional or active shells [4, 5, 6, 7, 8]. This concept motivated the design of multifunctional nanoparticles synthesized from disparate material systems as well as from doped materials. Given the multifunctional nature and expanded material toolbox, these nanoparticles have played a role in creating active drug delivery systems [9, 10], photocatalysis enhancers [11, 12, 13, 14, 15, 16], and sensing agents [17, 18, 19].

One particularly interesting core–shell structure is the Au core:ZnO shell nanosphere [20, 21, 22]. Gold nanospheres have a well-known surface plasmonic resonance effect (SPR) [23, 24, 25]. Given the stability of gold nanoparticles and nanostructures in air, the SPR behavior underpins many technological advances over the past two decades ranging from cloaking [26, 27, 28, 29] to biosensing [30, 31, 32]. Notably, because of their intrinsic stability, the development of a shell was not a critical hurdle to technology translation; thus, the development of synthesis strategies for gold core–shell nanoparticles has been an underexplored area of research despite its potential impact.

The ZnO shell material has similar environmental stability to gold nanoparticles and exhibits numerous unique physical characteristics. ZnO is a wide band gap semiconductor that is optically active in the ultraviolet regime and is interesting for its high exciton binding energy, which enables excellent optical characteristics at room temperature [33]. Very few materials possess this unique combination of properties. Therefore, this material has attracted significant interest in the research community, and many routes for synthesizing ZnO nanostructures, such as nanowires [34, 35] and nanotetrapods [36, 37], have been developed. Additionally, interesting behavior including high temperature ferromagnetism [38] and enhanced photocatalytic activity from doped ZnO nanomaterials has been shown [39].

https://doi.org/10.1557/jmr.2019.352 Published online by Cambridge University Press

© Materials Research Society 2019

Rare earth metal–doped ZnO nanoparticles have demonstrated unique properties in the past. These properties include enhanced sensing capabilities, antimicrobial activity, and band gap tunability [40, 41]. However, many of the past doped nanoparticle works have involved synthetic techniques with significant drawbacks, such as high temperature processing or a high degree of complexity [42]. In this work, we present a modification of the ascorbic acid–assisted synthetic technique, which is a low-temperature, one-pot procedure for producing ZnO nanoparticles and Au–ZnO core–shell nanoparticles with the option of including a rare earth metal dopant. This work is focused on demonstrating the feasibility of five different rare earth metal dopants, including Ce, Er, Nd, Tm, and Yb, and additionally, Cu as a control dopant.

Recently, Au–ZnO nanospheres were successfully synthesized using a new ascorbic acid–assisted synthetic technique, which eases lattice compatibility issues while retaining many of the optical properties of both materials [43]. The demonstration represented a significant advance in nanomaterial design, overcoming past hurdles related to difficulties encapsulating the gold nanoparticle directly in ZnO due to the lattice mismatch between gold and ZnO [44]. This strategy relies on first forming a self-assembled amorphous Zn mesh surrounding the gold nanoparticle, which is subsequently converted into ZnO through an annealing process, known as calcining [18]. The amorphous Zn mesh stage in the synthesis process opens the door to doping the ZnO shell with a wide range of secondary elements. However, minimal research has investigated the ability to create doped Au–ZnO core–shell structures. Additionally, the role of gold core in the ZnO shell formation and the degree of crystallinity of the ZnO shell have not been well-characterized.

In the present work, we demonstrate a strategy to incorporate metal dopants into the highly porous Zn-based mesh shell of the core–shell nanosphere (Fig. 1). Gold nanospheres served as a nucleation template for the metal-doped Zn-based mesh shells. To gain insight into the role of the gold core as a nucleation site, four different types of metal-doped Au–ZnO core–shell nanospheres were synthesized (Fig. 1). The different nanosphere architectures were selected to specifically investigate three related processes: (i) the role of the core and calcining in the core–shell nanosphere formation, (ii) the compatibility of different metal dopants with the shell material, and (iii) the effect of the metal dopant on the shell calcining process, especially at high dopant concentrations. The morphologies and nanoparticle size distributions were determined, dopant intercalation was verified, and the efficiency of dopant intercalation into the shell was measured for a wide range of metal dopants. Lastly, the conversion of the Zn-based mesh shell into ZnO via calcining was studied, along with the impact of the metal dopants on the resultant ZnO shell.

Results and discussion

The dopants tested in this work were a series of rare earth metals, namely, Ce, Er, Nd, Tm, and Yb, and additionally, Cu. The rare earth elements were chosen for their large atomic size and chemical dissimilarity to Zn, which made them excellent candidates to stress test the shell's ability to incorporate foreign dopants. To complement this set of rare earth metal dopants, we also used Cu. Because Cu is a common impurity in bulk ZnO, it is well known to intercalate with minimal impact on the crystal structure [45]. Therefore, it was an ideal control in the synthesis and contrasted with the large atomic size and chemical dissimilarity between the rare earth metal dopants and Zn.

As shown in Fig. 1, four different synthetic procedures that shared several features in common were performed, and particles were studied both before and after calcining. Figure 2 shows SEM images of all six types of metal-doped particles synthesized (pre-calcine). In the images, the spherical gold core is clearly visible, and the doped, Zn-based mesh shell is formed uniformly around the gold core.

To investigate the role of the gold core on particle formation, particles with and without the core were imaged using scanning electron microscopy (SEM), and the size distribution was analyzed using dynamic light scattering (DLS). Figure 3 includes a pair of SEM images showing 8% Cu-doped particles with and without a gold core. The particles without a gold core were typically larger and barrel-shaped when the dopant concentrations exceeded 6%, as seen in Figs. 3(a) and 3(c). In contrast, the particles with gold cores showed spherical symmetry with up to 10% doping (Cu). Higher dopant concentrations were also imaged via SEM, and it was found that significant particle morphological deformations occurred for most doped samples exceeding about 6% doping.

The particle size distributions observed in the SEM imaging were verified quantitatively with DLS. For core–shell particles, the average diameters varied between 60 and 250 nm over the range of Cu dopant concentrations studied, with no observable dependence on dopant concentration (Figs. 3, S1, and S2). Without the gold core, the size distribution was broader and the average diameter was twice as large as the average diameter of particles with the gold core [Fig. S3(a)], and many no-core particles were close to 1 μm in size (Figs. S1–S2). The polydispersity index of the particles was 10% lower on average with the gold core present compared with without a gold core, even as the concentration of the dopant increased [Fig. S3(b)]. Additionally, each rare earth dopant sample was tested at a concentration of 1% with a gold core; the resulting size distributions were similar to the 1% Cu-doped sample with a gold core (Fig. S4). Thus, it is plausible to expect similar

https://doi.org/10.1557/jmr.2019.352 Published online by Cambridge University Press

© Materials Research Society 2019

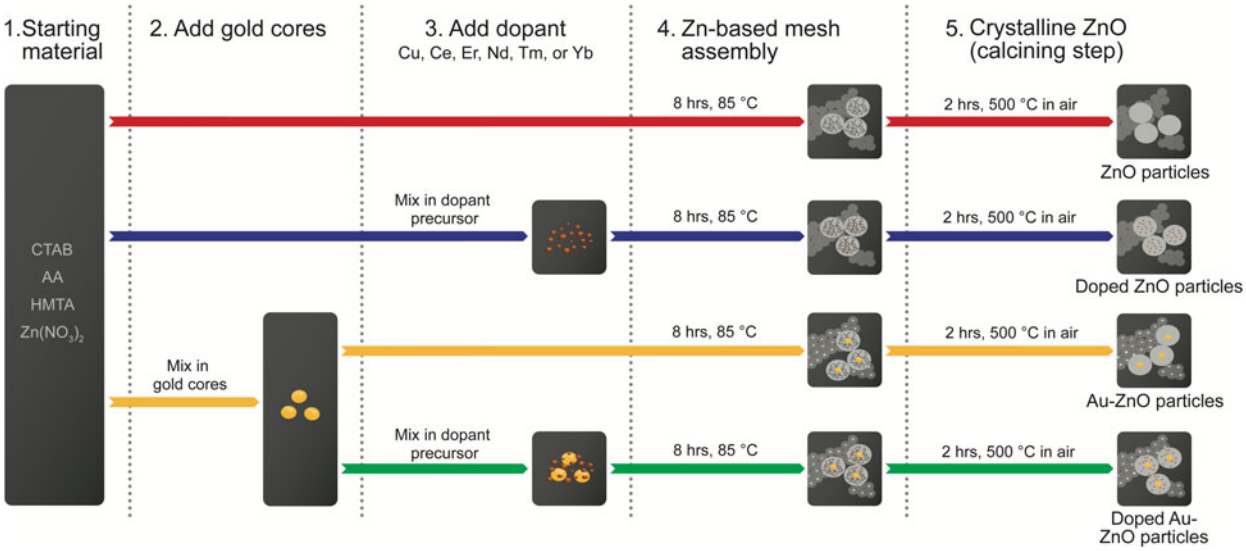


Figure 1: An overview of the design of experiments to rigorously investigate the role of the core on the particle formation, the compatibility with and impact of the dopants on the shell, and the effect of calcining on the doped core–shell nanoparticles. Four types of particles were synthesized: two with cores (yellow and green reaction pathways) and two without gold cores (red and blue reaction pathways). Of each type, one was doped with the metal precursor and one was not doped, resulting in the four unique types of particles in Column 4. The dopants investigated were Cu, Ce, Er, Nd, Tm, and Yb. These particles were then calcined to create the particles shown in Column 5.

interactions between each rare earth dopant and the gold core as between the Cu dopant and the gold core. By comparing the SEM images and DLS size distributions of particles with and without gold cores, it was evident that the gold core was playing a significant role in stabilizing the nanoparticle growth in the presence of dopants. This justified studying particles with and without gold cores.

This stabilization can be explained by viewing the role of the gold core as a nanotemplate for the formation of the Zn-based shell. As proposed by Yang et al. [43], the Zn shell is formed through a self-assembly process that begins with an initial loosely packed cetrimonium bromide (CTAB) layer on the gold nanoparticle surface, with the gold core influencing the layer formation and uniformity. This layer assembles into the meshed, disordered CTAB–$[AA\text{-}Zn(OH)_4]^{2-}$ complex. The dopants are unlikely to substitute a Zn site in the shell mesh because most of them are in the 3+ oxidation state when dissolved in the growth solution, leaving only porous spaces in the Zn-based mesh shell as intercalation sites. In the absence of a gold core, the Zn mesh formation was uncontrolled. Hence, in the absence of a gold core, the dopant wields greater influence over the morphology of the particle by occupying and distorting the flexible porous spaces in the mesh. This interaction was most evident at high dopant concentrations, where the dopant changed the particle morphology significantly. An example of this morphology change is shown in SEM images in Fig. 4 for 1 and 4% Ce-doped samples. Additional images for all dopants at additional concentrations are presented in Figs. S5–S11.

To evaluate the intercalation efficiency of the dopants into the ZnO shell, two types of electron microscopy with energy dispersive X-ray spectroscopy (EDX) analysis were performed. Together, the results of this analysis provided strong verification that dopants were intercalating into the shell. The first method used high spatial resolution transmission electron microscopy (TEM)-EDX to measure the distribution of the different elemental components within the nanospheres. Representative TEM-EDX images of the pre-calcine nanospheres doped with 4% of Ce or Nd are shown in Fig. 5. The Zn and dopant signals were clearly correlated in the shell, providing evidence for successful and uniform co-location of the dopant within the Zn-based shell mesh. This analysis showed qualitative spatial correlation between the dopant atoms and Zn atoms at the single nanoparticle level for each metal with a spectrally resolvable EDX signal (Figs. S12–S15). Unfortunately, spectrally resolvable signals were unable to be obtained for Cu and Er in the TEM because the TEM chamber contains Cu and Co. It was impossible to deconvolve the chamber and the dopant Cu signals. Additionally, the most intense spectral lines of Er (Er L family) overlap with the Co K family of spectral lines. These factors prevented qualitative spatial correlation of Cu or Er with Zn at the individual particle level. To verify that the Cu and Er dopant atoms were intercalated into the Zn shell, an additional quantitative experiment was required. This second analysis also provided an opportunity to investigate the efficiency of intercalation.

Although a known concentration of dopant was added during growth, the amount that intercalates into the particle

https://doi.org/10.1557/jmr.2019.352 Published online by Cambridge University Press

© Materials Research Society 2019

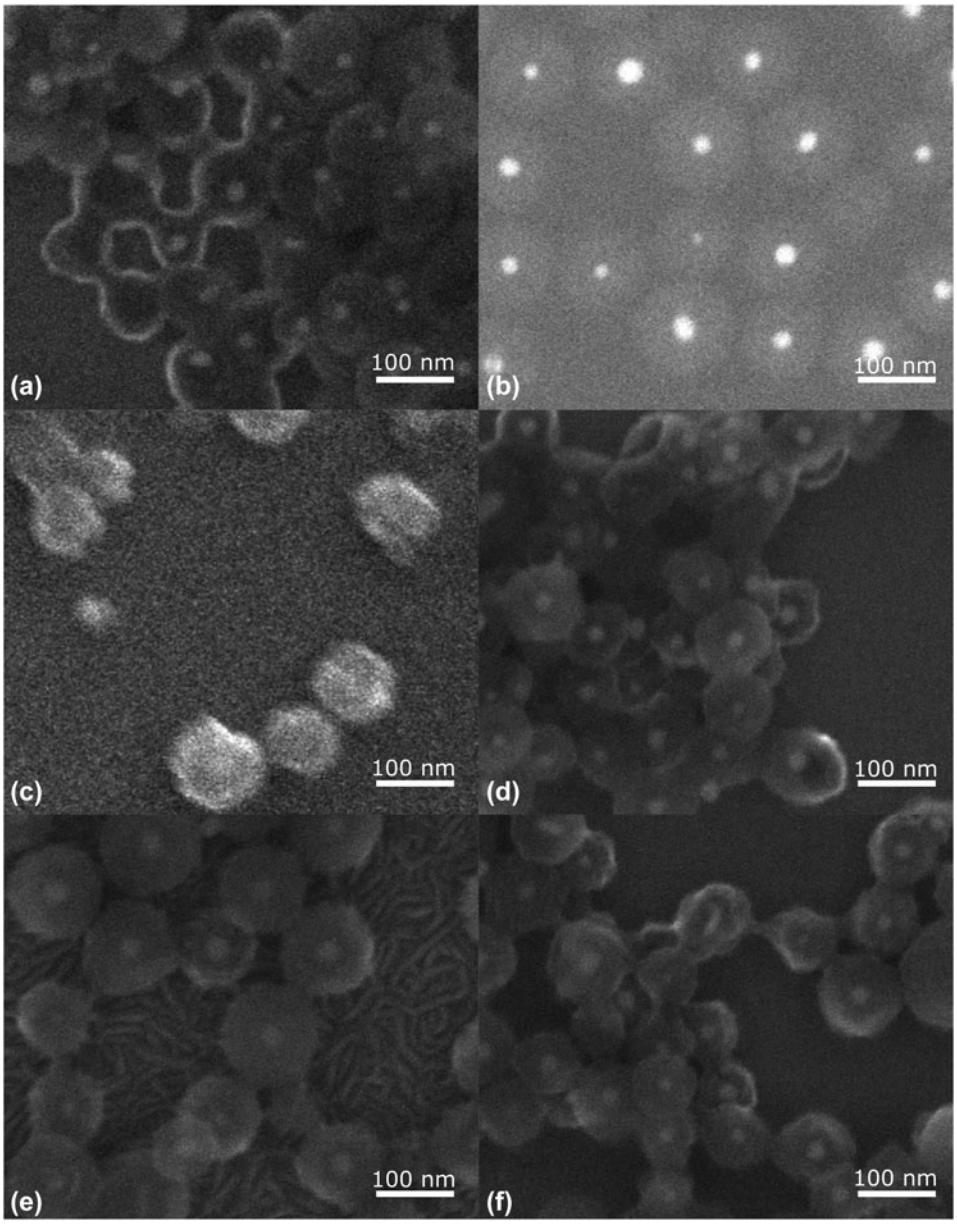


Figure 2: Representative SEM images showing successful core–shell nanoparticle formation. The nanoparticles are doped with 1% of (a) Yb, (b) Cu, (c) Nd, (d) Tm, (e) Ce, and (f) Er. Representative EDX spectra verifying the presence of the dopant are given in the Supplementary material.

shell may be different. However, at low to moderate dopant concentrations, the dopant concentration in the shell and the dopant concentration added to the solution should be linearly proportional. Therefore, any deviation from a linear relationship indicates nonuniform intercalation. To measure this ratio, SEM-EDX analysis on aggregates of nanoparticles with varying dopant concentrations was performed. While this method has lower spatial resolution than TEM-EDX, it allowed us to determine the composition with a low background. The ratio between the added and the measured dopant concentration provided information about the compatibility of each dopant with the nanoparticle shell's crystal structure and provided insight into the strength of the interaction between the dopant and the Zn present in the particle shell.

The quantitative SEM-EDX analysis of the nanoparticle aggregates showed clear linear relationships between the molar ratios added to the growth solution and the molar ratios measured by EDX for all dopants (Fig. 6). Based on good linear fits, the slope of the lines, or the intercalation efficiencies, for Cu, Ce, Er, Nd, Tm, and Yb were 1.00, 2.70, 1.30, 0.973, 1.71, and 2.31, respectively. This finding, together with the spatial co-location demonstrated with TEM-EDX and the morphological perturbations seen at high doping concentrations, provided strong evidence that dopant intercalation into

https://doi.org/10.1557/jmr.2019.352 Published online by Cambridge University Press

© Materials Research Society 2019

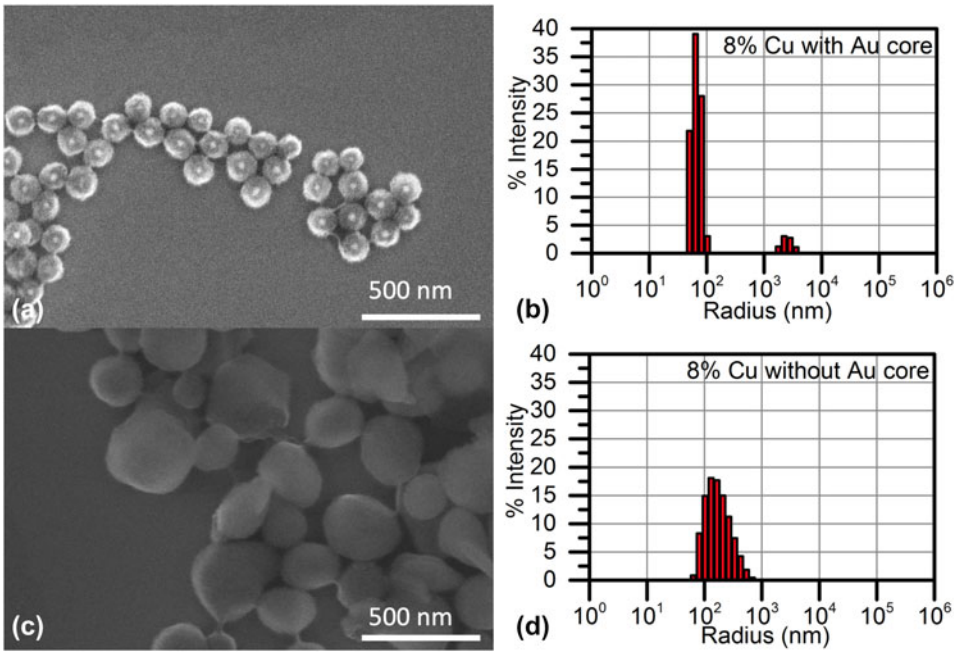


Figure 3: Impact of the gold core on the 8% Cu-doped particle formation. (a) and (b) SEM image and DLS results of the Cu-doped nanoparticles with a stabilizing gold core. The peak between 1,000 and 10,000 nm in the DLS results is attributed to micron-sized junk particles, which were visible in the SEM images. (c) and (d) SEM image and DLS results of the Cu-doped nanoparticles without a stabilizing gold core. Qualitatively, the general morphology of the particles was significantly more spherical with the addition of the core. Based on the DLS, the polydispersity index of the nanoparticles was, on average, 10% lower when a core was present. Additional DLS results are located in the Supplementary material.

the nanoparticle shell was successful. The ability to intercalate dopants into the shell is notable, given the high dopant concentrations studied in this work.

Previous works have mentioned the use of a post-synthesis calcining treatment when utilizing ascorbic acid–assisted Au–ZnO nanoparticles [18], but little work has been done to characterize the function of this calcining step, which is particularly relevant now that doped Au–ZnO nanoparticles are being synthesized. A key advantage of using the ascorbic acid–assisted synthetic technique is that the ZnO precursor is nucleated and then crystallized in two different steps. This approach makes the synthesis flexible to modification and allows for simple encapsulation of the gold core using a solution-based growth method. However, the lack of structural data motivated a more detailed investigation of the calcining process in both doped and undoped particles.

The first challenge in understanding the role of calcining in the shell formation is in identifying a sufficiently sensitive analytical technique. As can be observed in the SEM image in Fig. S16, the calcining process did not noticeably change the particle morphology, and thus, imaging provides little information. An alternative approach is to probe the crystalline nature of ZnO directly. Using ultraviolet–visible (UV-Vis) spectroscopy, the band edge absorption of ZnO, which should appear around 365 nm, can be measured [33]. An advantage of using this method is that it simultaneously provides information about the SPR wavelength of the gold core, which is also in the visible range (532 nm) [46]. As shown in Fig. 7, the absorption at 365 nm significantly increased after calcining, indicating the formation of a crystalline ZnO shell. In addition, the SPR wavelength of the gold core shifted from 532 to 562 nm (Fig. 7). Because the SPR wavelength is governed, in part, by the dielectric constant of the surrounding media [23], this increase in SPR wavelength indicates that the index of the shell increases. Therefore, this shift provides secondary confirmation that the shell converted into crystalline ZnO after the calcination process. However, this spectrum does not provide information regarding the polycrystallinity of the shell nor the appearance of new dopant phases at high doping levels.

An experiment to study the crystallinity of the shell pre- and post-calcine at different doping levels was thus performed. Powder XRD analysis was used on an undoped sample pre- and post-calcine as well as samples with 2 and 10% doping concentrations pre- and post-calcine, with the goal of identifying a change in the crystallinity of the shell and thus the impact of the dopant on the crystallinity. All measurements, including the undoped control sample pre- and post-calcine, are presented in Figs. S17–S23. For the pre-calcine undoped sample, the XRD pattern contained peaks associated with the gold core and the substrate, but peaks associated with ZnO formation were absent. In the case of the doped pre-calcine samples, regardless of doping concentration or dopant element

https://doi.org/10.1557/jmr.2019.352 Published online by Cambridge University Press

© Materials Research Society 2019

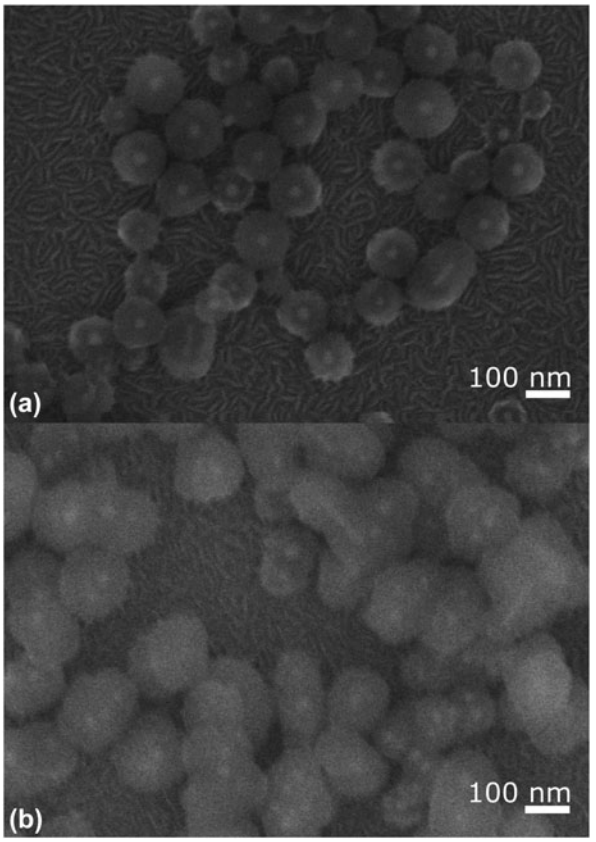


Figure 4: SEM images of (a) 1% and (b) 4% Ce-doped nanoparticles. The morphology becomes distinctly less spherical at the higher concentration due to the intercalation of large amounts of Ce dopant.

used, similar results were observed. In addition to the peaks associated with gold, faint peaks associated with $Zn(OH)_2$ were detected in the pre-calcine particle scans along with some very weak ZnO peaks. Therefore, it is possible to conclude that little to no ZnO formation happened naturally during the synthesis of the doped nanoparticle shell and that the calcining treatment converted the shell into ZnO.

After calcining the undoped sample, multiple wide peaks associated with crystalline ZnO appear, suggesting the formation of small ZnO crystalline phases and thus polycrystalline ZnO [47, 48, 49] (Fig. 8). Similar ZnO-related peaks were observed for all 2% doped and 10% doped samples. Because the undoped and 2% doped particles maintain their spherical morphology (Fig. S16), it can be hypothesized that these crystalline regions are in randomly distributed grains throughout the ZnO shell. In summary, post-calcine XRD peaks were extremely similar across most dopants and concentrations, with strong ZnO formation, and the disappearance of the weak peaks associated with $Zn(OH)_2$.

Given the high doping concentrations used, we expected to also observe new crystalline phases for all highly doped post-calcine particles. However, only the 10% Ce-doped ZnO produced an additional XRD peak that could be attributed to CeO_2 [Fig. 8(b)]. The thickness of the peaks indicates very small crystallite domains. Given the results from the quantitative composition measurements, which found that Ce has a significantly higher intercalation efficiency, it is not surprising that the Ce was able to phase separate from the ZnO at lower

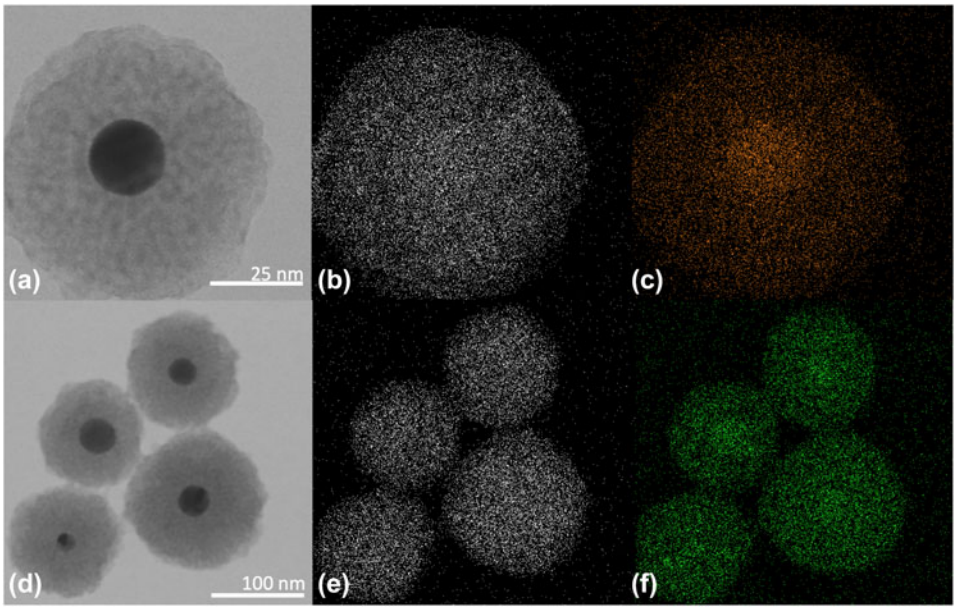


Figure 5: Qualitative correlative microscopy using TEM-EDX demonstrating incorporation of (a)–(c) 4% Nd and (d)–(f) 4% Ce. (a) and (d) TEM images of the core–shell nanoparticles. (b) and (e) The spatial EDX map of the Zn signal. (c) Spatial map of the EDX signal from Nd. (f) Spatial map of the EDX signal from Ce. There is a clear overlap of the EDX signal from the Zn and the metal dopant with the particle location in the TEM image. Images of additional dopants are given in the Supplementary material.

https://doi.org/10.1557/jmr.2019.352 Published online by Cambridge University Press

© Materials Research Society 2019

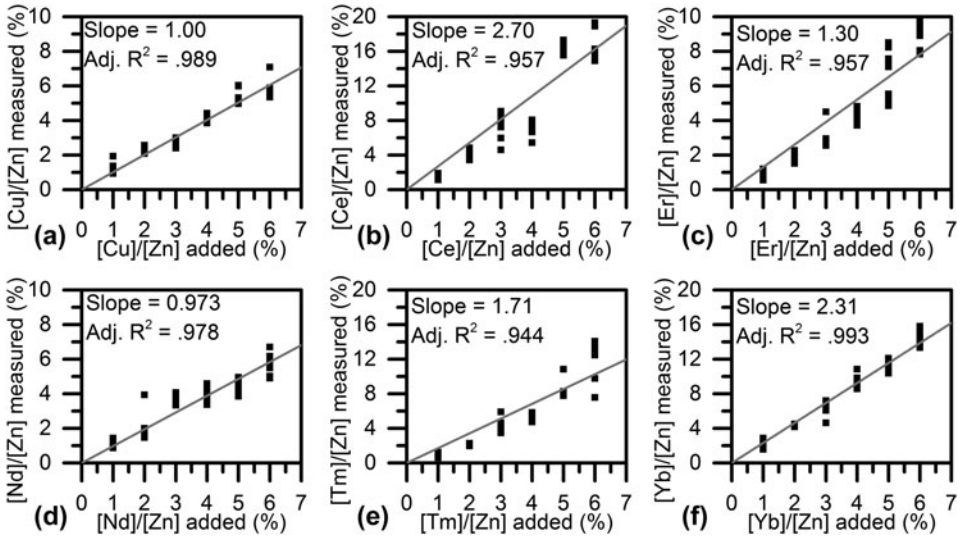


Figure 6: Fitted quantitative SEM-EDX measurements of the pre-calcine core–shell nanoparticle pellet aggregates to determine dopant intake. The dopants are (a) Cu, (b) Ce, (c) Er, (d) Nd, (e) Tm, and (f) Yb. Over the dopant concentration range synthesized, the concentration dependence is linear for all metals, providing support for the proposed self-assembly mechanism. At higher concentrations, where dopant–dopant or other interactions may begin to appear, deviations in this trend are expected. While still maintaining a linear dependence, Ce had the highest intercalation efficiency. These data demonstrate the feasibility of using a wide range of chemical elements as dopants.

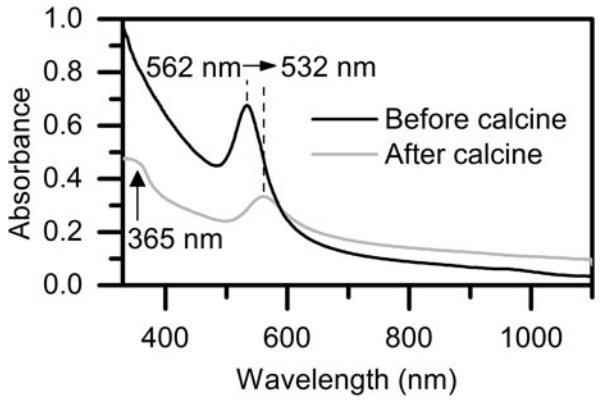


Figure 7: UV-Vis spectra of pre- and post-calcine particles. In the UV-Vis spectra, a red shift of the gold plasmonic resonance is seen and the appearance of a band-edge absorption peak associated with ZnO, confirming conversion of the shell material to ZnO.

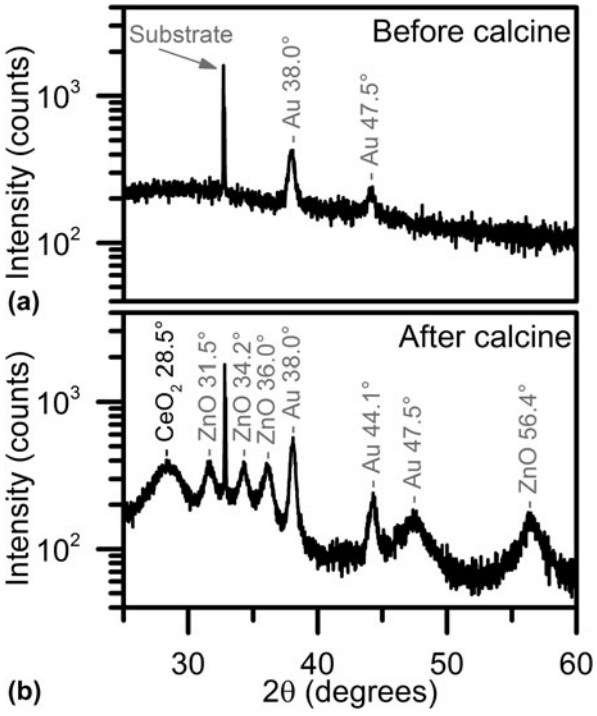


Figure 8: XRD pattern of a core–shell nanoparticle sample doped with 10% Ce (a) before and (b) after calcining. Before calcining, only the substrate and the gold nanoparticle cores were detected. After calcining, multiple peaks associated with ZnO are detected, along with a wide peak attributed to CeO_2. Additional XRD results are given in the Supplementary material.

concentrations than the other elements. As a result of this new phase, Ce-doped particles showed significant morphological changes with increasing dopant concentration (Figs. 4, S6, S24).

Conclusion

In this work, we have demonstrated a strategy for doping a wide range of metals into the Au–ZnO core–shell nanoparticle system while maintaining the crystalline ZnO shell. Doping is an important technique in many semiconductor and nanoparticle-based technologies, as it allows for the introduction of new material components to achieve flexibility and functionality. Our experiments provided insight into the effect of dopant atoms on particle morphology, and thus knowledge on where the dopants are intercalating. At low dopant concentrations, the gold core determines the void shapes, and thus spherical symmetry is maintained. However, at high dopant concentrations, the dopants begin to overcome the

https://doi.org/10.1557/jmr.2019.352 Published online by Cambridge University Press

© Materials Research Society 2019

stabilizing forces of the gold core and deform the voids of the shell, destabilizing the particle morphologies and size distributions. Furthermore, we verified that dopant intercalation can be successful for a wide variety of chemical elements and studied the crystallization process in doped systems. This work provides a foundation for the application of doped Au–ZnO core–shell nanoparticle systems in applications like sensing [17, 18, 19] and catalysis [11, 12, 13, 14, 15, 16].

Methods

The gold nanosphere synthesis method produces uniform gold nanospheres that are 40 nm in diameter and that are surface-functionalized with CTAB [50]. The procedure was carried out as follows. To produce 20 mL of gold nanospheres, a water bath was kept at kept at 30 °C, then 25 mL of 1 mM $HAuCl_4$ (99.995%; Honeywell) was added to 25 mL of 200 mM CTAB (99%; Amresco), and the mixture was placed in the water bath. This is called the growth solution. After gentle mixing, 350 μL of 78.8 mM ascorbic acid (AA) (99%; Sigma Life Sciences) was added to the growth solution, and the color changed from light yellow to clear. In a separate vial, also kept in the 30 °C water bath, a gold seed solution was prepared: 1 mL of 0.5 mM $HAuCl_4$ is added to 1 mL of 200 mM CTAB. A 10 mM $NaBH_4$ (96%; Aldrich) solution was prepared by adding the appropriate amount of $NaBH_4$ to ice-cold deionized water. The 10 mM $NaBH_4$ solution served as a reducing agent for the seed solution. When the $NaBH_4$ solution was added to the seed solution, the formation of small gold nanospheres occurs. Therefore, 120 μL of the 10 mM $NaBH_4$ solution was added to the seed solution, and the color of the seed solution changed from light yellow to light brown, indicating the formation of the cores. Immediately, 60 μL of the seed solution was transferred to the growth solution vial. Because the growth solution contained AA, the remainder of the $HAuCl_4$ precursor was reduced, and gold ion slowly nucleates on the gold seed crystals, producing a nanosphere within the CTAB micelle template. During this process, the growth solution was thoroughly mixed by shaking and was allowed to sit at 30 °C for up to half an hour. The reaction was done when the color changed from clear to pink, which was confirmed with UV-Vis spectroscopy.

To form the core–shell structure (Fig. 1), a growth solution containing CTAB, AA, methenamine (HMTA), and the Zn ion was mixed in a vial. In one vial, 206 μL of 266 mM CTAB and 220 μL of 50 mM AA were added to 17.34 mL of deionized water. Then, 110 μL of 500 mM Zn nitrate hexahydrate (99%; Alfa Aesar) was added. If a metal dopant was being used, we added a variable volume of 27.5 mM: copper(II) chloride (98%; Alfa Aesar), cerium(III) nitrate hexahydrate (99.99%; Reacton), erbium(III) nitrate pentahydrate (99.99%; Alfa Aesar), neodymium(III) nitrate hydrate (99.99%; Reacton), thulium(III) nitrate hydrate (99.99%; Reacton), or ytterbium(III) nitrate hydrate (99.99%; Alfa Aesar). At this scale, 1% added corresponds to 20 μL of the corresponding metal precursor solution. Finally, 1.1 mL of 50 mM HMTA (Sigma-Aldrich, 99%) was added along with the gold core solution.

The mixture is then heated at 85 °C for 8 h, and the resulting particles have Zn-based mesh shells. Finally, to convert the shell into ZnO, all particles were calcined at 500 °C for 2 h in air at ambient pressure.

It is important to note that the core–shell synthesis conditions were optimized to have an excess of cores, and thus nucleation sites, to avoid homogeneous Zn-based particle formation. Therefore, not all cores formed shells. Additionally, before adding to the growth solution vial, the gold nanoparticle cores were 2× washed via centrifugation at 21,000 relative centifugal force (RCF). To one 20 mL batch of core–shell nanoparticle growth solution, we added 1 mL of gold nanoparticles that has been 10× concentrated from the as-made concentration described previously. This concentration was determined to be suitable such that every particle has a gold core, verified by SEM imaging. The finished, pre-calcine particles were thoroughly centrifuged and decanted to remove any excess reactants, ensuring that the metal detected in EDX analysis could not be remaining solution precursor. Calcined particle samples were prepared by drying out the particles on a hot plate and then transferring the particles to a tube furnace. The calcination process was done at 500 °C in air, for 2 h, with a 15-min ramp up from room temperature and then air cooled.

Zn-based mesh nanoparticles without gold cores were also synthesized using the same synthesis procedures, replacing the gold core addition with 1 mL of deionized water.

All UV-Vis spectra were obtained using a Beckman Coulter DU-730 UV Vis Spectrometer. UV-Vis spectra of the particles were taken when the particles were dispersed in the solution and after the centrifugation process mentioned previously. SEM images were taken using an FEI Nova NanoSEM, and quantitative EDX spectra were obtained using ThermoFisher UltraDry 100 mm^2 Windowless EDX. All SEM was done after the centrifugation process described above, and the washed particles were dried out on a piece of silicon wafer for imaging. TEM images were taken on the JEOL JEM-2100F TEM, and spatial correlation EDX measurements were acquired using Oxford Xmax TLE 100 mm^2 windowless EDX. The TEM grids used were SiN TEM grids (SN100-A10Q33B, SiMPore). XRD spectra were captured on the Bruker D8 advance using a 1600 W beam at 1.54 Å wavelength. XRD were captured between 5° and 60° as the nanoparticle signal was faint against the silica/silicon background and could not be resolved above 60°. XRD samples were prepared by concentrating 20 mL of as-made core–shell nanoparticles onto a small (2 cm × 2 cm)

https://doi.org/10.1557/jmr.2019.352 Published online by Cambridge University Press

© Materials Research Society 2019

piece of silicon wafer. The DLS measurements were acquired on Mobius Zetasizer from Wyatt Technology.

Acknowledgments

We would like to thank our funding agencies, as this work was supported by the Office of Naval Research (N000141712270) and the Army Research Office (W911NF1810033). We would also like to thank Matthew Mecklenburg and Tom Orvis at the USC Core Center of Excellence in Nano Imaging for their assistance with TEM EDX data collection, and Mark Veksler of the USC Iovine and Young Academy for the graphical art and schematic.

Supplementary material

To view supplementary material for this article, please visit https://doi.org/10.1557/jmr.2019.352.

References

1. **B.O. Dabbousi, J. Rodriguez-Viejo, F.V. Mikulec, J.R. Heine, H. Mattoussi, R. Ober, K.F. Jensen, and M.G. Bawendi**: (CdSe) ZnS core–shell quantum dots: Synthesis and characterization of a size series of highly luminescent nanocrystallites. *J. Phys. Chem. B* **101**, 9463 (1997).
2. **X. Peng, M.C. Schlamp, A.V. Kadavanich, and A.P. Alivisatos**: Epitaxial growth of highly luminescent CdSe/CdS core/shell nanocrystals with photostability and electronic accessibility. *J. Am. Chem. Soc.* **119**, 7019 (1997).
3. **M.A. Hines and P. Guyot-Sionnest**: Synthesis and characterization of strongly luminescing ZnS-capped CdSe nanocrystals. *J. Phys. Chem.* **100**, 468 (1996).
4. **J.M. Chan, L. Zhang, K.P. Yuet, G. Liao, J-W. Rhee, R. Langer, and O.C. Farokhzad**: PLGA–lecithin–PEG core–shell nanoparticles for controlled drug delivery. *Biomaterials* **30**, 1627 (2009).
5. **R. Haag**: Supramolecular drug-delivery systems based on polymeric core–shell architectures. *Angew. Chem., Int. Ed.* **43**, 278 (2004).
6. **T. Chen, T. Zhao, D. Wei, Y. Wei, Y. Li, and H. Zhang**: Core–shell nanocarriers with ZnO quantum dots-conjugated Au nanoparticle for tumor-targeted drug delivery. *Carbohydr. Polym.* **92**, 1124 (2013).
7. **O. Chen, J. Zhao, V.P. Chauhan, J. Cui, C. Wong, D.K. Harris, H. Wei, H-S. Han, D. Fukumura, R.K. Jain, and M.G. Bawendi**: Compact high-quality CdSe–CdS core–shell nanocrystals with narrow emission linewidths and suppressed blinking. *Nat. Mater.* **12**, 445 (2013).
8. **N-H. Cho, T-C. Cheong, J.H. Min, J.H. Wu, S.J. Lee, D. Kim, J-S. Yang, S. Kim, Y.K. Kim, and S-Y. Seong**: A multifunctional core–shell nanoparticle for dendritic cell-based cancer immunotherapy. *Nat. Nanotechnol.* **6**, 675 (2011).
9. **J. Dobson**: Magnetic nanoparticles for drug delivery. *Drug Dev. Res.* **67**, 55 (2006).
10. **H. Kang, A.C. Trondoli, G. Zhu, Y. Chen, Y-J. Chang, H. Liu, Y-F. Huang, X. Zhang, and W. Tan**: Near-infrared light-responsive core–shell nanogels for targeted drug delivery. *ACS Nano* **5**, 5094 (2011).
11. **Z. Xu, M. Quintanilla, F. Vetrone, A.O. Govorov, M. Chaker, and D. Ma**: Harvesting lost photons: Plasmon and upconversion enhanced broadband photocatalytic activity in core@shell microspheres based on lanthanide-doped $NaYF_4$, TiO_2, and Au. *Adv. Funct. Mater.* **25**, 2950 (2015).
12. **K. Maeda, K. Teramura, D. Lu, N. Saito, Y. Inoue, and K. Domen**: Noble-metal/Cr_2O_3 core/shell nanoparticles as a cocatalyst for photocatalytic overall water splitting. *Angew. Chem., Int. Ed.* **45**, 7806 (2006).
13. **J. Li, S.K. Cushing, J. Bright, F. Meng, T.R. Senty, P. Zheng, A.D. Bristow, and N. Wu**: Ag@Cu_2O core–shell nanoparticles as visible-light plasmonic photocatalysts. *ACS Catal.* **3**, 47 (2013).
14. **B. Li, T. Gu, T. Ming, J. Wang, P. Wang, J. Wang, and J.C. Yu**: (Gold core)@(ceria shell) nanostructures for plasmon-enhanced catalytic reactions under visible light. *ACS Nano* **8**, 8152 (2014).
15. **B. Li, R. Wang, X. Shao, L. Shao, and B. Zhang**: Synergistically enhanced photocatalysis from plasmonics and a co-catalyst in Au@ZnO–Pd ternary core–shell nanostructures. *Inorg. Chem. Front.* **4**, 2088 (2017).
16. **X. Liu, J. Iocozzia, Y. Wang, X. Cui, Y. Chen, S. Zhao, Z. Li, and Z. Lin**: Noble metal–metal oxide nanohybrids with tailored nanostructures for efficient solar energy conversion, photocatalysis and environmental remediation. *Energy Environ. Sci.* **10**, 402 (2017).
17. **Q. Zhang, G. Xie, H. Du, J. Yang, Y. Su, H. Tai, M. Xu, and K. Zhao**: Adsorption behaviors of gas molecules on the surface of ZnO nanocrystals under UV irradiation. *Sci. China Technol. Sci.* **62**, 1–10 (2019).
18. **F-C. Chung, Z. Zhu, P-Y. Luo, R-J. Wu, and W. Li**: Au@ZnO core–shell structure for gaseous formaldehyde sensing at room temperature. *Sens. Actuators, B* **199**, 314 (2014).
19. **S.M. Majhi, P. Rai, and Y-T. Yu**: Facile approach to synthesize Au@ZnO core–shell nanoparticles and their application for highly sensitive and selective gas sensors. *ACS Appl. Mater. Interfaces* **7**, 9462 (2015).
20. **K.K. Haldar, T. Sen, and A. Patra**: Au@ZnO core–shell nanoparticles are efficient energy acceptors with organic dye donors. *J. Phys. Chem. C* **112**, 11650 (2008).
21. **L. Sun, G. Wei, Y. Song, Z. Liu, L. Wang, and Z. Li**: Solution-phase synthesis of Au@ZnO core–shell composites. *Mater. Lett.* **60**, 1291 (2006).
22. **X. Shao, B. Li, B. Zhang, L. Shao, and Y. Wu**: Au@ZnO core–shell nanostructures with plasmon-induced visible-light

https://doi.org/10.1557/jmr.2019.352 Published online by Cambridge University Press

© Materials Research Society 2019

photocatalytic and photoelectrochemical properties. *Inorg. Chem. Front.* **3**, 934 (2016).

23. **S. Eustis and M.A. El-Sayed**: Why gold nanoparticles are more precious than pretty gold: Noble metal surface plasmon resonance and its enhancement of the radiative and nonradiative properties of nanocrystals of different shapes. *Chem. Soc. Rev.* **35**, 209 (2006).
24. **K.L. Kelly, E. Coronado, L.L. Zhao, and G.C. Schatz**: The optical properties of metal nanoparticles: The influence of size, shape, and dielectric environment. *J. Phys. Chem. B* **107**, 668 (2003).
25. **N.J. Halas, S. Lal, W-S. Chang, S. Link, and P. Nordlander**: Plasmons in strongly coupled metallic nanostructures. *Chem. Rev.* **111**, 3913 (2011).
26. **A. Alù and N. Engheta**: Plasmonic and metamaterial cloaking: Physical mechanisms and potentials. *J. Opt. A: Pure Appl. Opt.* **10**, 093002 (2008).
27. **W. Cai, U.K. Chettiar, A.V. Kildishev, and V.M. Shalaev**: Optical cloaking with metamaterials. *Nat. Photonics* **1**, 224 (2007).
28. **C. Argyropoulos, P-Y. Chen, F. Monticone, G. D'Aguanno, and A. Alù**: Nonlinear plasmonic cloaks to realize giant all-optical scattering switching. *Phys. Rev. Lett.* **108**, 263905 (2012).
29. **D. Schurig, J.J. Mock, B.J. Justice, S.A. Cummer, J.B. Pendry, A.F. Starr, and D.R. Smith**: Metamaterial electromagnetic cloak at microwave frequencies. *Science* **314**, 977 (2006).
30. **J.M. Pingarrón, P. Yáñez-Sedeño, and A. González-Cortés**: Gold nanoparticle-based electrochemical biosensors. *Electrochim. Acta* **53**, 5848 (2008).
31. **J. Liu and Y. Lu**: A colorimetric lead biosensor using DNAzyme-directed assembly of gold nanoparticles. *J. Am. Chem. Soc.* **125**, 6642 (2003).
32. **Y. Li, H.J. Schluesener, and S. Xu**: Gold nanoparticle-based biosensors. *Gold Bull.* **43**, 29 (2010).
33. **A. Janotti and C.G. Van de Walle**: Fundamentals of zinc oxide as a semiconductor. *Rep. Prog. Phys.* **72**, 126501 (2009).
34. **L.E. Greene, B.D. Yuhas, M. Law, D. Zitoun, and P. Yang**: Solution-grown zinc oxide nanowires. *Inorg. Chem.* **45**, 7535 (2006).
35. **M.H. Huang**: Room-temperature ultraviolet nanowire nanolasers. *Science* **292**, 1897 (2001).
36. **Z. Chen, Z. Shan, M.S. Cao, L. Lu, and S.X. Mao**: Zinc oxide nanotetrapods. *Nanotechnology* **15**, 365 (2004).
37. **V.M. Diep and A.M. Armani**: Flexible light-emitting nanocomposite based on ZnO nanotetrapods. *Nano Lett.* **16**, 7389 (2016).
38. **J.B. Wang, G.J. Huang, X.L. Zhong, L.Z. Sun, Y.C. Zhou, and E.H. Liu**: Raman scattering and high temperature ferromagnetism of Mn-doped ZnO nanoparticles. *Appl. Phys. Lett.* **88**, 252502 (2006).
39. **M.G. Nair, M. Nirmala, K. Rekha, and A. Anukaliani**: Structural, optical, photo catalytic and antibacterial activity of ZnO and Co doped ZnO nanoparticles. *Mater. Lett.* **65**, 1797 (2011).
40. **N. Koshizaki and T. Oyama**: Sensing characteristics of ZnO-based NO_x sensor. *Sens. Actuators, B* **66**, 119 (2000).
41. **A. Manikandan, E. Manikandan, B. Meenatchi, S. Vadivel, S.K. Jaganathan, R. Ladchumananandasivam, M. Henini, M. Maaza, and J.S. Aanand**: Rare earth element (REE) lanthanum doped zinc oxide (La: ZnO) nanomaterials: Synthesis structural optical and antibacterial studies. *J. Alloys Compd.* **723**, 1155 (2017).
42. **F. Jiang, Z. Peng, Y. Zang, and X. Fu**: Progress on rare-earth doped ZnO-based varistor materials. *J. Adv. Ceram.* **2**, 201 (2013).
43. **Y. Yang, S. Han, G. Zhou, L. Zhang, X. Li, C. Zou, and S. Huang**: Ascorbic-acid-assisted growth of high quality M@ZnO: A growth mechanism and kinetics study. *Nanoscale* **5**, 11808 (2013).
44. **P. Li, Z. Wei, T. Wu, Q. Peng, and Y. Li**: Au–ZnO hybrid nanopyramids and their photocatalytic properties. *J. Am. Chem. Soc.* **133**, 5660 (2011).
45. **S. Singhal, J. Kaur, T. Namgyal, and R. Sharma**: Cu-doped ZnO nanoparticles: Synthesis, structural and electrical properties. *Phys. B* **407**, 1223 (2012).
46. **S.J. Oldenburg, R.D. Averitt, S.L. Westcott, and N.J. Halas**: Nanoengineering of optical resonances. *Chem. Phys. Lett.* **288**, 243 (1998).
47. **S.C. Abrahams and J.L. Bernstein**: Remeasurement of the structure of hexagonal ZnO. *Acta Crystallogr., Sect. B: Struct. Crystallogr. Cryst. Chem.* **25**, 1233 (1969).
48. **E.A. Owen and E.L. Yates**: XLI. Precision measurements of crystal parameters. *London, Edinburgh Dublin Philos. Mag. J. Sci.* **15**, 472 (1933).
49. **R. Stahl, C. Jung, H.D. Lutz, W. Kockelmann, and H. Jacobs**: Kristallstrukturen und wasserstoffbrückenbindungen bei β-$Be(OH)_2$ und ε-$Zn(OH)_2$. *Z. Anorg. Allg. Chem.* **624**, 1130 (1998).
50. **B. Nikoobakht and M.A. El-Sayed**: Preparation and growth mechanism of gold nanorods (NRs) using seed-mediated growth method. *Chem. Mater.* **15**, 1957 (2003).

https://doi.org/10.1557/jmr.2019.352 Published online by Cambridge University Press

© Materials Research Society 2019